J. Fluid Mech. (1985), *vol.* 152, *pp.* 337–359
Printed in Great Britain

The large-scale coherent structure in the intermittent region of the self-preserving round free jet

By SATORU KOMORI AND HIROMASA UEDA
Division of Atmospheric Environment, The National Institute for Environmental Studies, Ibaraki 305, Japan

(Received 24 June 1983 and in revised form 16 July 1984)

Large-scale coherent structure in a round free jet injected into a low-speed, co-flowing stream was experimentally investigated using laser-Doppler and cold-wire techniques. Particular attention was paid to the coherent structures in the outer intermittent region of the jet in an almost self-preserving state. Velocity fluctuations u (axial) and v (radial) and temperature fluctuations θ were measured simultaneously at two positions: a reference position and a moving position. In order to clarify the pattern of coherent motion, a pattern-averaging technique was adopted and the characteristics of the turbulent fluctuations were conditionally averaged. The results show that a large-scale coherent structure exists even in the self-preserving region of a round free jet, as well as in the near field. It has a vortical structure which consists of strong outward turbulent motion from inside the jet, turbulent reverse flow and inflow in the irrotational ambient region (entrainment). In the coherent structure, the negative pattern-averaged Reynolds stress occurs at two locations: one in the irrotational ambient region outside the turbulent/irrotational interface and the other in the turbulent jet inside the interface. The former is instantaneously produced in the irrotational inflow outside the interface when the vortical motion is accelerated, and it changes even the sign of conventionally averaged Reynolds stress. The latter is instantaneously produced in the turbulent flow near the high-shear region when the turbulent motion is more strongly directed by the acceleration of the vortical motion towards the centre of the vortical structure than the averaged motion.

1. Introduction

Round free jets occur in many industrial processes and fluid-handling equipment. Investigation of the large-scale coherent structure of these flows in the outer intermittent region is of importance in relation to the problems of modelling of free shear flows and reactive–diffusive jets appearing in combustion flames and chemical reactors. For non-premixed reactive jets, the chemical reaction rate reaches a maximum in the intermittent region and large-scale coherent structures control the reaction rate and mixing (Komori & Ueda 1984).

To date, there have been a number of investigations of turbulence structures in round free jets. Corrsin (1943) originally investigated the problem, and Wygnanski & Fiedler (1969) and others continued the analysis using conventionally averaged turbulence quantities. Antonia, Prabhu & Stephenson (1975) and Sreenivasan, Antonia & Britz (1979) investigated large-scale structures in a heated round jet by using a conditional sampling technique. From their measurements it has been

recognized that large-scale motion has a significant effect on heat and momentum transport in the intermittent region. In addition, Chevray & Tutu (1978) conditionally detected the directions of fluid motion in the turbulent and irrotational zones and clarified the contributions of large-scale and small-scale motion to heat and momentum transfer. These investigations were, however, based on one-point measurements, not numerous enough to educe the spatial flow structure. In addition to visual observations of such flows, two-point measurements have been performed in the near field of round free jets by using two hot-wires (Bruun 1977; Yule 1978; Hussain & Zaman 1980, 1981). Bruun (1977) discovered coherent structures in the near field ($1.0 < x/d < 2.5$) by means of a new experimental time-domain technique (a special conditional sampling technique). Yule (1978) proved the existence of vortex rings in a relatively short transitional region, dependent on the Reynolds number, near the nozzle; and showed that large-scale coherent structures are produced by the deformation process caused by the entanglement of streets of vortex rings in the turbulent mixing region. However, Bruun (1977) and Yule (1978) could not obtain detailed spatial structures, since their measuring and ensemble-averaging techniques were not precise enough to characterize coherent structures without the occurrence of dispersion. Hussain & Zaman (1980, 1981) have conducted experiments in a round jet under controlled excitation and have explored the coherent structure dynamics in the near field by using a phase-averaging technique. Their results showed that controlled excitation enabled the accurate eduction of coherent structures which had not been detected in an unexcited flow. However, it should be noted that in their experiments only the axial velocity signal U at a reference (fixed) position was used for detecting coherent motion. If other turbulence signals in addition to the U-signal are simultaneously measured at the reference position, it may be possible to educe accurately coherent structures even in unexcited flow. Furthermore, it should be emphasized that all recent works deal with coherent structures only in the near field. The existence of coherent structures in the self-preserving region where the flow structures are free from initial conditions is still an open question. Consequently, investigating whether coherent structures continue to exist even into the self-preserving region is significant for the understanding and modelling of free shear flows.

The purpose of this study is to explore experimentally the existence of large-scale coherent structures in the intermittent region of a round free jet in an almost self-preserving state by using both a modified eduction technique and conditional sampling. As mentioned above, the eduction techniques adopted by Bruun (1977), Yule (1978) and Hussain & Zaman (1980, 1981) seem to be insufficient to distinguish the signal of coherent motion from background noise due to random motion. When both axial and radial velocities U_f and V_f are measured at a reference position, it may be possible to detect the direction of a large-scale eddy passing a reference measurement position. In addition, if the jet is slightly heated, simultaneous measurement of the passive temperature T_f will allow discrimination between turbulent jet fluid and irrotational ambient fluid passing a reference point. To obtain stable coherent structures the ambient fluid should have a small co-flowing velocity rather than being stagnant, since disturbances, such as those originating from flow stagnation and obstructions downstream, would possibly disperse the signal of coherent motion. Therefore, in this research, a slightly heated round jet injected into a low-speed, irrotational, co-flowing stream was chosen, and the velocities U (axial) and V (radial) and temperatures T were simultaneously measured both at a reference measurement position and a moving measurement position by using two laser-Doppler anemometers (LDA) and two resistance thermometers. In particular, the velocity measurements

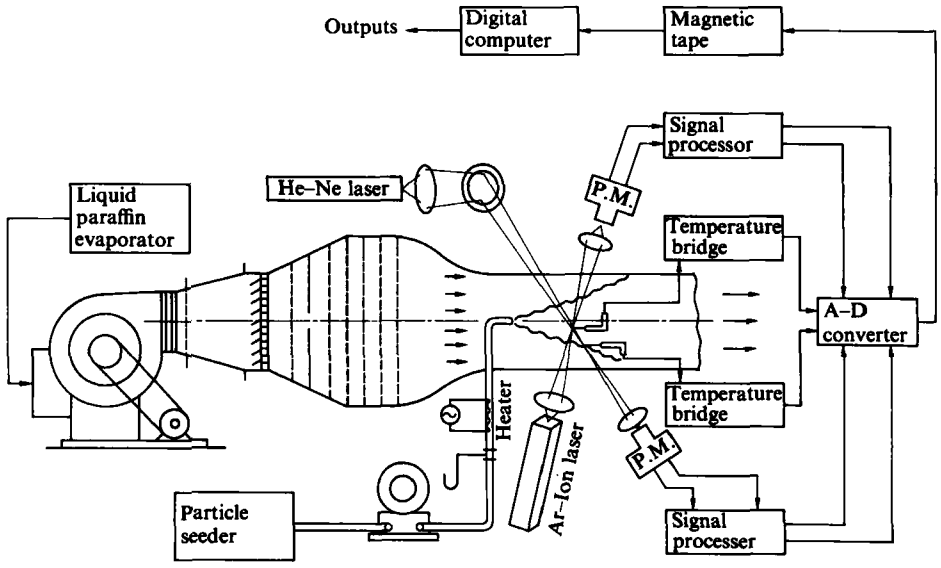

FIGURE 1. Experimental apparatus and instruments.

by the LDA are more effective than those by the hot-wire anemometer (HWA), since in the outer intermittent region of the self-preserving jet the existence of flow reversal is expected and it cannot be accurately detected by the HWA. In addition, the LDA is advantageous for a slightly heated jet because temperature compensation is not necessary.

In addition to the two-point measurements of U, V and T, a pattern-averaging (conditional sampling) technique was used to educe coherent structures. Based on the pattern-averaged turbulence characteristics, the existence of coherent structures and their shapes, sizes and orientations were investigated.

2. Experiment

2.1. *Jet arrangement*

The experimental apparatus used here was the same as used by Komori & Ueda (1984). Figure 1 shows schematically the experimental apparatus and instruments employed in the present investigation. A jet was generated by means of a radial blower with adjustable speed and heated electrically to a temperature $\overline{T}_p = 317$ K (20 K above ambient), before entering a stainless steel convergence nozzle with exit diameter $d = 0.01$ m. The jet velocity $\overline{U}_p$ was maintained at a constant velocity of 16.1 m/s, so that the Reynolds number at the jet exit was 9280. The r.m.s. values of the longitudinal and radial velocity fluctuations on the jet axis at the nozzle exit were 3% and 2.6% of $\overline{U}_p$ respectively. The jet was injected into an irrotational, co-flowing ambient stream moving at a constant low-speed, $\overline{U}_a = 0.15$ m/s, and constant temperature, $\overline{T}_a = 297$ K, in a low-speed, open-circuit wind tunnel with test section 1.0×1.5 m and 19 m long. The velocity of the co-flow $\overline{U}_a$ was rather low compared with the jet velocity $\overline{U}_c$ on the axis, and the velocity ratios $\overline{U}_c/\overline{U}_a$ were respectively 107 and 11 at the nozzle exit and at $\bar{x}/d = 50$. The intensities of the axial and radial velocity fluctuations in the co-flow were less than 0.09% of $\overline{U}_p$, and the correlation between the two velocity fluctuations was negligibly small. These

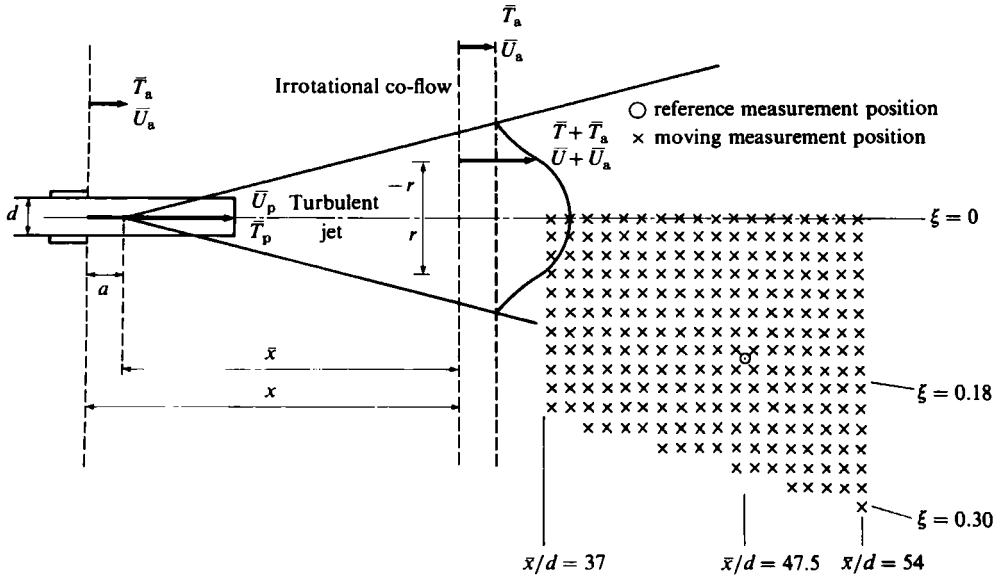

FIGURE 2. Scheme of the present jet and measuring positions.

conditions of the co-flow supported the view that it was sufficiently irrotational and enabled the present free jet to become self-preserving in the far region. Also, the co-flow possessed three advantages: continuous seeding in the ambient co-flowing stream for the LDA measurements; easy distinction between turbulent jet fluid and irrotational ambient fluid by contaminating the jet fluid with high temperature; and elimination of all the room draughts.

2.2. *Measurement and processing*

Figure 2 shows the scheme of the present round free jet and the measuring positions. The mean and fluctuating velocities and temperatures were measured simultaneously at two positions in the slightly heated jet. One is a reference (fixed) measurement position at $\bar{x}/d = 47.5$ and $\xi = 0.18$, where $\bar{x}$ is the distance measured in the downstream direction relative to a virtual origin. The non-dimensional radial distance ξ is defined by the ratio of the distance r from the axis of symmetry to the distance $\bar{x}$. The reference measurement position is in the outer intermittent region of the jet where turbulence characteristics are almost self-preserving. In the outer intermittent region turbulent (jet) and irrotational (ambient co-flow) fluids pass intermittently and successively, which can be most clearly distinguished by the temperature signal θ. The other measurement position – moving (non-fixed) measurement position – was moved in the spatial region enclosed by $37 \leqslant \bar{x}/d \leqslant 54$ and $0 \leqslant \xi \leqslant 0.3$ on the (x, r)-plane with the reference measurement point. 240 measurement locations were selected with a separation distance of 0.01 m in the axial and radial directions.

Two velocity components in the directions oriented at $\pm 45°$ to the axial (x-) direction were simultaneously measured with two laser-Doppler anemometers both at a reference position and at a moving position. By summing and differencing the two velocity components recorded on a magnetic digital tape, the axial and radial velocity components, U and V, were computed, as in hot-wire anemometry. The optical system used at the moving measurement positions was a DISA 55X Two

Colour optics with the 40 MHz Bragg cell and beam expander. The laser used here was a Spectra-Physics 4 W Ar-Ion laser (Model 165-08). This optical system was positioned by a traversing mechanism. The other optical system used at a reference measurement position was a DISA 55X Modular optics with a polarization beam splitter (55X24), 40 MHz Bragg cell and beam expander, and the laser used was a Spectra-Physics 15 mW He–Ne laser (Model 124). These LDA units were used in the forward-scatter mode with their optical axes perpendicular to the (x, r)-plane. The beam spacing was 0.0524 m and the focal length of the achromatic front lens was 1 m for both optical arrangements. This gave a measuring volume in the form of an ellipsoid of 0.00023 m diameter and 0.009 m length, and a fringe spacing of 12 μm. The scattered light was detected by four photomultipliers (DISA 55X08) with a DISA 55X35 colour separator for the Two-Colour LDA system; and with a DISA 55X39 polarization separator for the Modular LDA system. The photomultiplier signals were simultaneously processed by four frequency trackers (DISA 55N20). The ambient stream was seeded by premixing a mist of liquid paraffin. For the slightly heated jet, a medical powder (Riyukakusan Co. Ltd), dispersed by an O.E.I. solid particle seeder, was used as scattering particles to avoid the change of the particles by electric heating.

Mean and fluctuating temperatures, $\bar{T}$ and θ, were measured by using two DISA 55P11 cold-wire probes of diameter 5 μm operated by a DISA 55M20 constant current temperature bridge both at a reference measurement position and at a moving measurement position, simultaneously with the velocity measurements. This technique for the simultaneous measurements of velocity and temperature was also used by Komori & Ueda (1984) and Komori *et al.* (1982, 1983). The moving probe could be positioned accurately to within 0.0005 m downstream of the measuring volume of the LDA by a three-dimensional traversing mechanism using pulse motors.

The signals from these instruments were directly transmitted to a digital recorder (TEAC DR-2000) through analog low-pass filters (WAVETEK Model 852) and stored on a magnetic tape. The analog filters were used to cut off the velocity signals higher than 200 Hz, which were contaminated with the broadening. From the sampling theorem in the frequency domain, the sampling interval required to describe the fluctuations with the frequencies of 0–200 Hz is 0.0025 s (see Bendat & Piersol 1971). Therefore the sampling interval was set at 0.002 s and a sample size of 90000 was adopted. Statistical processing and conditional sampling of the digitized data recorded on the magnetic tape were made with the HITAC M-180 computer system. In particular, the drop-out signal was rejected by the computer processing method presented by Mizushina *et al.* (1979).

2.3. *Accuracy of measurements*

Accuracy of velocity measurements

To reduce biasing errors due to non-uniformities of particle concentration in the measuring volume, the particle concentration was controlled so as to keep the scattered-light intensity to an equal value between the jet and co-flowing stream. The biasing errors could be estimated by seeding the unheated jet with the same concentration particles as in the ambient co-flow. The uniform seeding for the jet was achieved by sucking the ambient fluid which was seeded by a mist of liquid paraffin from the contraction chamber before the test section of a wind tunnel. Under the uniform-seeding conditions, the mean velocity, the r.m.s. values of the axial and radial velocity fluctuations u and v, and the Reynolds stress $\overline{uv}$ were measured in the intermittent region. The comparison of these values with the measurements in the

same intermittent region of the unheated jet seeded by two different particles (a mist of liquid paraffin and a medical powder) showed that in the present measurements the maximum errors due to the biasing effect are $\pm 0.28\,\%$ for the maximum mean velocity, $\pm 0.46\,\%$ for the maximum r.m.s. values and $\pm 0.67\,\%$ for the maximum Reynolds stress, in the region of $37 \leqslant \bar{x}/d \leqslant 54$.

The present long control volume of 0.00023 m diameter and 0.009 m length causes broadening effects. In the present measurements, the effects due to both finite transit time broadening and instrument broadening were found to be negligible from estimation-equations given by Durst, Melling & Whitelaw (1976). Similarly, the errors due to the velocity gradient in the control volume were estimated to be less than $\pm 0.4\,\%$ for the maximum mean velocity and $\pm 0.09\,\%$ for the maximum r.m.s. value of velocity fluctuation in the outer intermittent region of $37 \leqslant \bar{x}/d \leqslant 54$. Compared with these broadening effects, the turbulence-broadening effect becomes rather significant for small-scale turbulent fluctuations with high frequencies. In order to estimate the turbulence-broadening error, the axial velocity fluctuation u was measured up to the high-frequency range of 2 kHz in the unheated jet by using a hot-wire probe (DISA 55P11) in conjunction with the constant-temperature anemometer (DISA 55M10). The comparison of the power spectra measured at the same position by two anemometers (HWA and LDA) showed that the turbulence broadening becomes significant in the frequency range higher than 200 Hz. In the present measurements, the LDA signals higher than 200 Hz were cut off by using analog low-pass filters before digitization and the sampling interval of 0.002 s also acted as a digital filter which cut off the frequency components higher than 250 Hz (see Bendat & Piersol 1971). Thus, the turbulence broadening effect, and so small-scale fluctuations could be neglected in the frequency range higher than 250 Hz. To estimate the error due to this procedure (turbulence broadening), the power spectra measured up to 1 kHz by the LDA and by the HWA were integrated from 0.1 to 250 Hz and from 0.1 Hz to 1 kHz, respectively. From the comparison of the integrated values, the errors due to the turbulence broadening were estimated to be less than $\pm 1.02\,\%$ for the maximum r.m.s. value of velocity fluctuation in the region of $37 \leqslant \bar{x}/d \leqslant 54$. By assuming a constant correlation between u and v in the whole frequency range, the turbulence broadening error for the maximum Reynolds stress in the region of $37 \leqslant \bar{x}/d \leqslant 54$ was estimated to be less than $\pm 2.04\,\%$. The turbulence-broadening effect on the mean velocity was negligible.

In the present measurements, the average number density of scattering particles was approximately 3×10^{10} particles/m^3, so that the average rate of signals received from particles crossing the scattering volume was estimated to be 2.174×10^5 Hz from the relation given by Durst *et al.* (1976). The rate was larger than the third order of magnitude of the highest turbulence frequency (200 Hz) in the present jet. This means that the particle arrival rate is sufficient.

The diameter and density of the scattering particles were about 5 μm and 420 kg/m^3, respectively. According to the estimation equation presented by Melling & Whitelaw (1975), the frequency response of the particles was estimated to be 9.35 kHz. This frequency was far larger than the maximum frequency of the turbulence signals in the present jet, so that the particle lag effects could be neglected.

By summing up the above errors, the maximum errors by the LDA measurements were estimated to be $\pm 0.68\,\%$ for the maximum mean velocity, $\pm 1.57\,\%$ for the maximum r.m.s. value of velocity fluctuations and $\pm 2.71\,\%$ for the maximum Reynolds stress, in the region of $37 \leqslant \bar{x}/d \leqslant 54$. These errors will be shown in subsequent figures, except for figure 6 (*a*), by the size of the symbol.

Accuracy of temperature measurements

In the case of turbulent heat fluxes, the errors due to the temperature measurements by a cold-wire are added. The frequency response of the cold-wire (DISA 55P11) was estimated to be about 200 Hz from the power spectra of the temperature fluctuation (Komori & Ueda 1984), which was sufficient for the present measurements. However, the errors due to the sensitivity of the cold-wire could not be neglected in the far-downstream region. The errors due to this sensitivity were estimated to be less than $\pm 2\%$ for the r.m.s. values of the temperature fluctuation and $\pm 1\%$ for the mean temperature. From these errors, together with the errors for the velocity measurements, the errors for the turbulent heat fluxes were estimated approximately to be less than $\pm 3.6\%$. These errors will also be shown in subsequent figures (except for figure 6*a*) by the size of the symbol.

3. Conditional averaging techniques

The conditional averaging techniques attempted here are zone-averaging and pattern-averaging. The zone-averages for a quantity Q are defined by

$$\langle Q\rangle_{\mathrm{t}} = \overline{QI(t)}/\overline{I(t)}, \tag{1}$$

$$\langle Q\rangle_{\mathrm{i}} = \overline{Q(1-I(t))}/\overline{(1-I(t))}, \tag{2}$$

and the zone-averages of the cross-correlation of fluctuating quantities p and q are defined by

$$\langle pq\rangle_{\mathrm{t}} = \overline{(P-\langle P\rangle_{\mathrm{t}})\,(Q-\langle Q\rangle_{\mathrm{t}})\,I(t)}/\overline{I(t)}, \tag{3}$$

$$\langle pq\rangle_{\mathrm{i}} = \overline{(P-\langle P\rangle_{\mathrm{i}})\,(Q-\langle Q\rangle_{\mathrm{i}})\,(1-I(t))}/\overline{(1-I(t))}, \tag{4}$$

where the function $I(t)$ is the intermittency function for the zone-average. The symbols $\langle\ \rangle_{\mathrm{t}}$ and $\langle\ \rangle_{\mathrm{i}}$ and overbar ($\bar{}$) indicate the average over the turbulent jet zone only, the average over the irrotational zone only, and the conventional time-average, respectively.

The intermittency function $I(t)$ is set to 1 when the flow is turbulent and to zero when it is irrotational. In this study $I(t)$ was determined only from the temperature signal, similar to the procedure described by Antonia, Prabhu & Stephenson (1975). The use of the temperature signal is very advantageous for flow in which the turbulent diffusion is far larger than the molecular diffusion, and it is widely used for many heat-transfer experiments. Whenever the instantaneous temperature in the intermittent region was higher than the temperature of the ambient irrotational co-flowing stream, the flow fluid was considered turbulent and $I(t)$ was set to 1. In order to allow for the noise level of the temperature signal, $I(t)$ was determined as follows:

$$I(t) = \begin{cases} 1 & \text{when } \theta(t) \geqslant \theta_{\min} + Th_1(\overline{T}_{\mathrm{c}} - \overline{T}_{\mathrm{a}}) \quad (\xi > 0.16), \\ & \theta(t) \geqslant \theta_{\min} + Th_2\theta' \qquad (\xi \leqslant 0.16), \\ 0 & \text{when } \theta(t) < \theta_{\min} + Th_1(\overline{T}_{\mathrm{c}} - \overline{T}_{\mathrm{a}}) \quad (\xi > 0.16), \\ & \theta(t) < \theta_{\min} + Th_2\theta' \qquad (\xi \leqslant 0.16), \end{cases} \tag{5}$$

where $\theta(t)$ is the temperature fluctuation, $\overline{T}_{\mathrm{c}}$ the mean temperature on the axis, θ' the root mean squared value of $\theta(t)$, and Th_1 and Th_2 are the thresholds given by $Th_1 = 0.1$ and $Th_2 = 1.5$. Also, the symbol $\theta_{\min}$ means the negative minimum value of the instantaneous temperature fluctuation and the sum of $\theta_{\min}$ and the mean temperature $\overline{T}$ approximately corresponds to the temperature of the ambient stream.

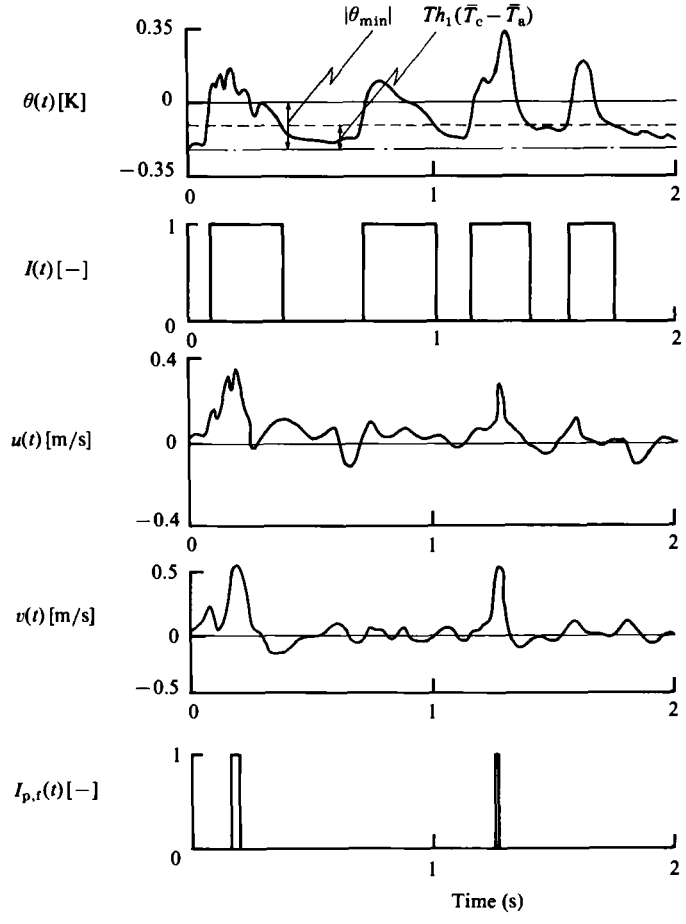

FIGURE 3. Simultaneous recording of the instantaneous values of $\theta(t)$, $I(t)$, $u(t)$, $v(t)$ and $I_{p,r}(t)$ at a reference position ($\xi = 0.18$ and $\bar{x}/d = 47.5$).

To remove the effect of low-frequency trend, θ_{min} was determined from a minimum value of θ-signal every 2 s (a short time interval). This scheme becomes clearer in the time-records of the temperature signal $\theta(t)$ and $I(t)$ at the reference measurement position of $\bar{x}/d = 47.5$ and $\xi = 0.18$ (figure 3). A dot–dash line shows the level of θ_{min}. To test the validity of the present $I(t)$, the time-averaged value of $I(t)$, the so-called intermittency factor f, was computed and shown in figure 4. The radial distribution of f is in good agreement with those obtained by Wygnanski & Fiedler (1969) from the velocity signals. This suggests that the present simple turbulence-detection scheme is sufficient.

In addition to the intermittent positive turbulent signal of the temperature fluctuation $\theta(t)$, intermittent positive spikes of the axial and radial velocity fluctuations, $u(t)$ and $v(t)$, can be observed simultaneously in the intermittent region, as shown in figure 3. This suggests that a strong outward large-scale turbulent motion towards the ambient irrotational stream exists in the intermittent region. As will be shown later, this outward motion is approximately directed towards the reference measurement position.

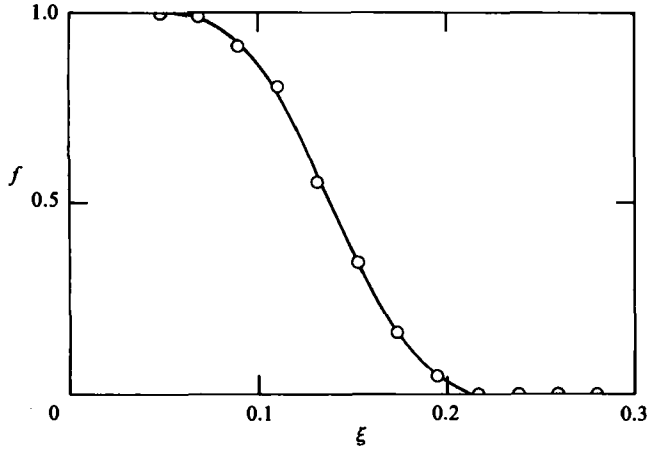

FIGURE 4. Radial distribution of the intermittency factor: ○, present data; ——, data of Wygnanski & Fiedler (1969).

By assuming that coherent motion only accompanies this strong outward turbulent motion at the reference measurement position, the other intermittency function, $I_{\mathrm{p,f}}(t)$, was defined by the following scheme:

$$I_{\mathrm{p,f}}(t) = \left\{ \begin{matrix} 1 & \text{only when } J(t) = 1,\ u_{\mathrm{f}}(t) \geqslant Th_3 u'_{\mathrm{f}} \text{ and } v_{\mathrm{f}}(t) \geqslant Th_3 v'_{\mathrm{f}}, \\ 0 & \text{otherwise,} \end{matrix} \right\} \tag{6}$$

where $u_{\mathrm{f}}(t)$ and $v_{\mathrm{f}}(t)$ are the axial and radial velocity fluctuations at the reference measurement position respectively, and u'_{f} and v'_{f} are the r.m.s. values of $u_{\mathrm{f}}(t)$ and $v_{\mathrm{f}}(t)$. The function $J(t)$ in (6) is defined by

$$J(t) = \left\{ \begin{matrix} 1 & \text{when } I_{\mathrm{f}}(t) = 1 \text{ and } \theta_{\mathrm{f}}(t) \geqslant Th_3 \theta'_{\mathrm{f}}, \\ 0 & \text{when } I_{\mathrm{f}}(t) = 1 \text{ and } \theta_{\mathrm{f}}(t) < Th_3 \theta'_{\mathrm{f}} \text{ or } I_{\mathrm{f}}(t) = 0, \end{matrix} \right\} \tag{7}$$

where θ'_{f} is the r.m.s. value of the temperature fluctuation at the reference position θ_{f}, and $I_{\mathrm{f}}(t)$ is the value of $I(t)$ at the reference position. The value of the threshold Th_3 was set to 0.5. This detection scheme shows that $I_{\mathrm{p,f}}(t)$ is set to 1 whenever a strong part of the outward turbulent motion (a clear pattern) occurs at the reference measurement position of $\bar{x}/d = 47.5$ and $\xi = 0.18$ (figure 3). Thus, the average defined by $I_{\mathrm{p,f}}(t)$ was called the 'pattern-average'. The pattern-averages for a quantity Q and the cross-correlation of fluctuating quantities p and q are given by

$$\langle Q \rangle_{\mathrm{p}} = \overline{QI_{\mathrm{p,f}}(t)} / \overline{I_{\mathrm{p,f}}(t)}, \tag{8}$$

$$\langle pq \rangle_{\mathrm{p}} = \overline{(P - \langle P \rangle_{\mathrm{p}})(Q - \langle Q \rangle_{\mathrm{p}}) I_{\mathrm{p,f}}(t)} / \overline{I_{\mathrm{p,f}}(t)}. \tag{9}$$

The above threshold values $Th_1 (= 0.1)$ and $Th_2 (= 1.5)$ were determined by plotting the average frequencies F of $I(t)$ against Th_1 and Th_2, respectively. The frequencies nondimensionalized by $\bar{U}_{\mathrm{p}}/d$ are shown in figure 5. In each graph of F versus Th_1 or Th_2 there exists a plateau where F becomes reasonably constant (this is also found in the study by Antonia, Prabhu & Stephenson 1975). In this plateau region, the maximum values of Th_1 or Th_2 were selected as the threshold values. For the values of $Th_1 = 0.1$ and $Th_2 = 1.5$, the average frequency of $I_{\mathrm{p,f}}(t)$ was calculated and also plotted against Th_3 in figure 5. The threshold value of $Th_3 = 0.5$ was selected, based

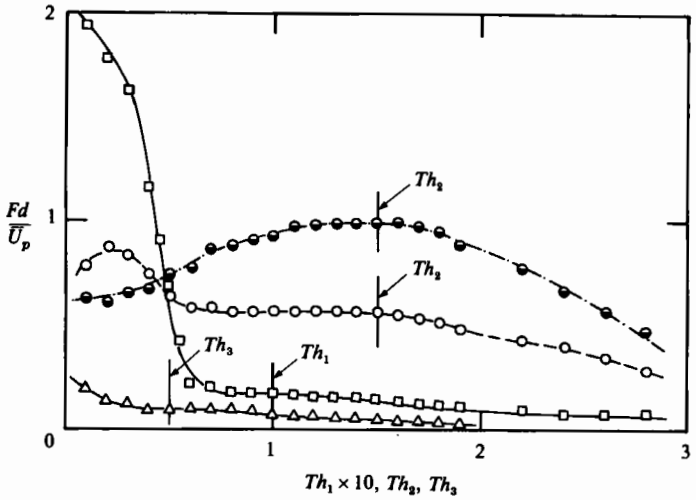

FIGURE 5. Effects of thresholds Th_1, Th_2 and Th_3 on the average frequencies of $I(t)$ and $I_{p,f}(t)$ at $\bar{x}/d = 47.5$: □, Th_1, $\xi = 0.18$; ○, Th_2, $\xi = 0.15$; ◒, Th_2, $\xi = 0.12$; △, Th_3, $\xi = 0.18$.

on the fact that the average frequency of $I_{p,f}(t)$ has a plateau in the range of $0.4 < Th_3 < 0.6$.

In addition to $I_{p,f}(t)$, the other intermittency functions $I_{p2,f}(t)$, $I_{p3,f}(t)$ and $I_{p4,f}(t)$ were determined to investigate the existence of other coherent structures:

$$I_{p2,f}(t) = \begin{cases} 1 & \text{only when } J(t) = 1,\ u_f(t) \leqslant -Th_3 u_f' \text{ and } v_f(t) \geqslant Th_3 v_f', \\ 0 & \text{otherwise,} \end{cases} \tag{10}$$

$$I_{p3,f}(t) = \begin{cases} 1 & \text{only when } J(t) = 1,\ u_f(t) \leqslant -Th_3 u_f' \text{ and } v_f(t) \leqslant -Th_3 v_f', \\ 0 & \text{otherwise,} \end{cases} \tag{11}$$

$$I_{p4,f}(t) = \begin{cases} 1 & \text{only when } J(t) = 1,\ u_f(t) \geqslant Th_3 u_f' \text{ and } v_f(t) \leqslant -Th_3 v_f', \\ 0 & \text{otherwise.} \end{cases} \tag{12}$$

However, any other coherent structures could not be clearly detected from the pattern-averages by $I_{p2,f}(t)$, $I_{p3,f}(t)$ and $I_{p4,f}(t)$. This suggests that, in the interval between one coherent outward motion detected by $I_{p,f}(t)$ and the next, any other expected coherent turbulent motions do not appear clearly. Thus, in the present study, only a pattern-average by $I_{p,f}(t)$ in (6) was used to educe a coherent structure.

4. Results and discussion

4.1. *Conventional averaged quantities*

Figures 6(*a*) and (*b*) show the variations of the mean axial velocity $\overline{U}$ and mean temperature $\overline{T}$ along the axis of the jet and their radial distributions. The abscissa $\bar{x}(= x+a)$ was measured in the downstream direction relative to a virtual origin a, determined from the decay of the mean velocity and temperature on the axis of the jet. In the present jet, the value of a was approximately equal to $-3d$. In the far-field

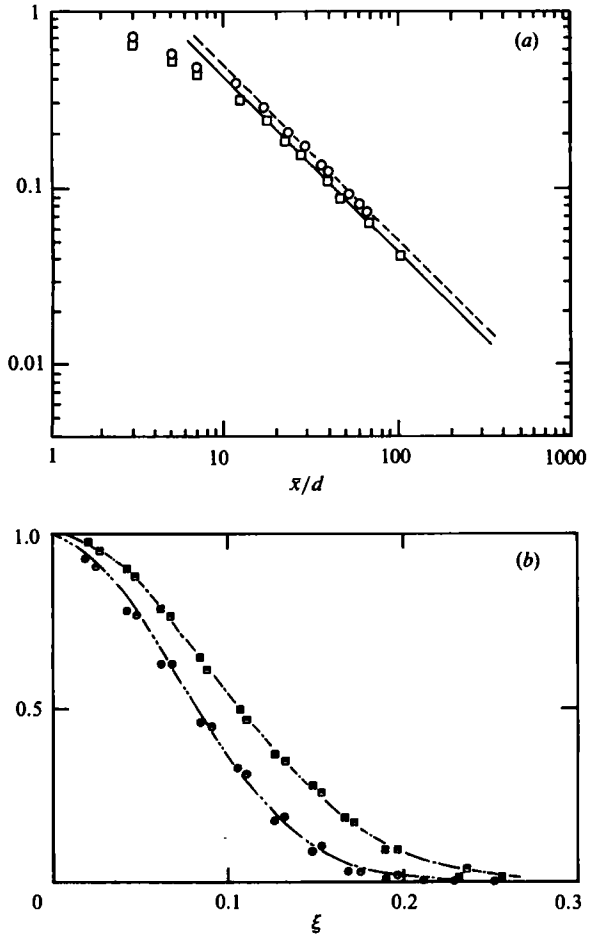

FIGURE 6. Distributions of axial mean velocity and temperature: (*a*) axial distributions: ○, $(\bar{U}_c-\bar{U}_a)/(\bar{U}_p-\bar{U}_a)$; □, $(\bar{T}_c-\bar{T}_a)/(\bar{T}_p-\bar{T}_a)$; – – –, equation (13); ——, equation (14); (*b*) radial distributions: ● $(\bar{x}/d=47.5)$, ◓ $(\bar{x}/d=37.5)$, $(\bar{U}-\bar{U}_a)/(\bar{U}_c-\bar{U}_a)$; ■ $(\bar{x}/d=47.5)$, ◨ $(\bar{x}/d=37.5)$, $(\bar{T}-\bar{T}_a)/(\bar{T}_c-\bar{T}_a)$; –··–, equation (15); –·–, equation (16).

region of $\bar{x}/d>20$, the velocity and temperature profiles on the axis become self-preserving and are represented by

$$(\bar{U}_c-\bar{U}_a)/(\bar{U}_p-\bar{U}_a)=5.0d/\bar{x}, \tag{13}$$

$$(\bar{T}_c-\bar{T}_a)/(\bar{T}_p-\bar{T}_a)=4.3d/\bar{x}. \tag{14}$$

Subscripts a, c and p denote the values in the ambient irrotational co-flow, on the jet axis and at the nozzle exit respectively. The decay constants are similar to the measurements by other investigators, and detailed comparisons are available elsewhere (Komori & Ueda 1984). Radial distributions of the mean velocity also become similar in the far-field region of $\bar{x}/d>20$ and they are well correlated by the following exponential curves:

$$(\bar{U}-\bar{U}_a)/(\bar{U}_c-\bar{U}_a)=\exp(-100\xi^2), \tag{15}$$

$$(\bar{T}-\bar{T}_a)/(\bar{T}_c-\bar{T}_a)=\exp(-60\xi^2). \tag{16}$$

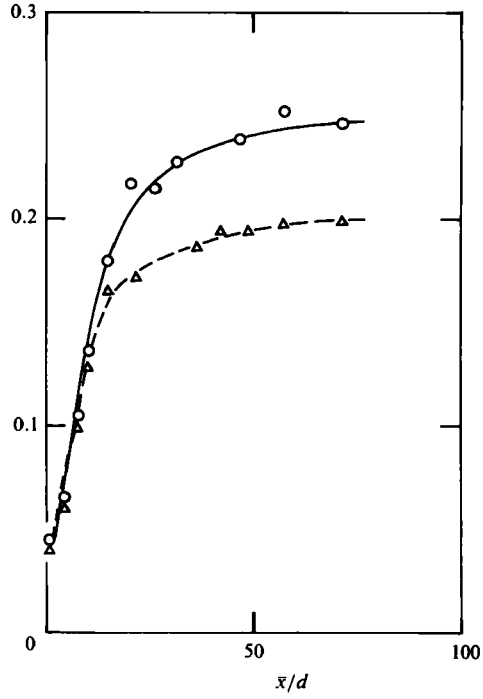

FIGURE 7. Distributions of the turbulence intensities of the axial and radial velocity fluctuations along the axis of the jet: ○, $u'/(\bar{U}_c - \bar{U}_a)$; △, $v'/(\bar{U}_c - \bar{U}_a)$.

Figure 7 shows the turbulence intensities (r.m.s. values) of the axial and radial velocity fluctuations, u' and v', along the axis of the jet. Both the intensities rapidly increase in the near field of $\bar{x}/d < 30$, and approach constant values of $u'/(\bar{U}_c - \bar{U}_a) = 0.25$ and $v'/(\bar{U}_c - \bar{U}_a) = 0.20$ in the far field of $\bar{x}/d > 30$. This fact, together with the mean velocity profiles in figure 6, show that the present jet is not perfectly self-preserving in the region of $37 \leqslant \bar{x}/d \leqslant 54$, but is almost in a self-preserving state. This also supports the view that the effects of the irrotational co-flow are so small that the present jet can be treated as a self-preserving jet in a quiescent environment.

Figure 8 shows the radial distributions of the turbulent heat fluxes and momentum flux (Reynolds stress) in the almost self-preserving region of $\bar{x}/d = 47.5$. In the outer region of $\xi \gtrsim 0.21$, the turbulent heat fluxes in the axial and radial directions, $\overline{u\theta}$ and $\overline{v\theta}$, become almost zero, as does the intermittency factor f (see figure 4). This suggests that the value of $\xi \approx 0.21$ corresponds to the conventionally averaged location of the outer edge of the turbulent jet, i.e. the turbulent–irrotational interface. In the region near the interface, $0.18 < \xi < 0.25$, the Reynolds stress $\overline{uv}$ has negative values and it attains the negative maximum at $\xi \approx 0.21$, where a small velocity gradient exists (see figure 6*b*). This means that energy is damped in the region near the interface. This negative Reynolds stress has not been observed in the measurements of Chevray & Tutu (1978) and others. This may be attributed partly to the difficulties of velocity measurement by the hot-wire technique. The hot-wire output does not respond linearly to the instantaneous velocity in the outer region where the mean velocity is small and flow reversal will be present. In fact, a similar change of sign of $\overline{uv}$ has been measured in the mixing layer (Wygnanski & Oster 1980) where the mean

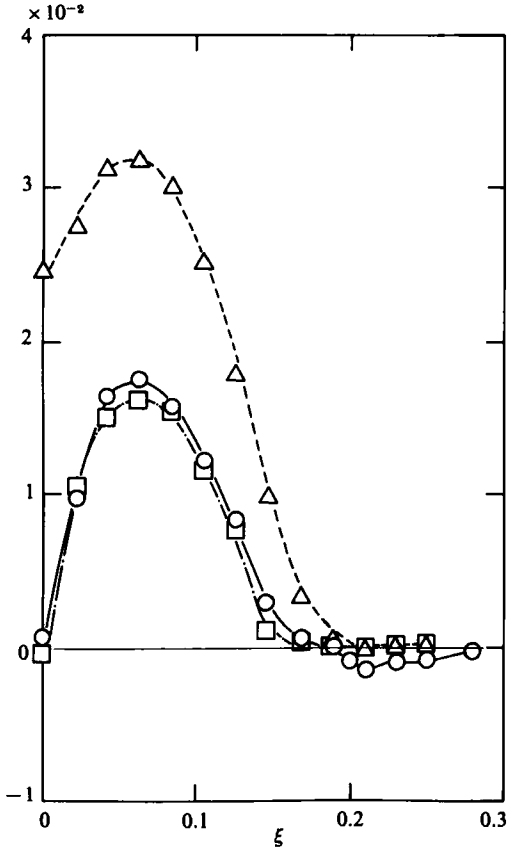

FIGURE 8. Radial distributions of Reynolds stress and axial and radial turbulent heat fluxes at $\bar{x}/d = 47.5$;

$-\bigcirc-$, $\overline{uv}/(\bar{U}_c - \bar{U}_a)^2$; $--\triangle--$, $\overline{u\theta}/[(\bar{U}_c - \bar{U}_a)(\bar{T}_c - \bar{T}_a)]$; $-\cdot-\square-\cdot-$, $\overline{v\theta}/[(\bar{U}_c - \bar{U}_a)(\bar{T}_c - \bar{T}_a)]$.

velocity is large and hot-wire anemometry is applicable. Consequently, it is suspected that the present change of sign of $\overline{uv}$ may be caused by a coherent motion which will be present in the self-preserving jet, as in the case of the mixing layer. The generation mechanism of the negative $\overline{uv}$ will be discussed later.

4.2. *Radial distributions of the zone-averaged fluxes*

The turbulent and irrotational zone-averaged heat and momentum fluxes are shown in figures 9(*a*), (*b*) and (*c*). From the turbulent zone-averaged fluxes $\langle v\theta \rangle_t$ and $\langle u\theta \rangle_t$, it is found that the heat is transferred only by turbulent motion in the interface (outer edge) region where $0.18 < \xi < 0.25$. In the region in which $\xi > 0.25$, where the intermittency factor f is eventually equal to zero, both $\langle v\theta \rangle_t$ and $\langle u\theta \rangle_t$ become zero. This indicates that the turbulent eddy hardly plunges into that region which is regarded as the completely irrotational region outside the jet. The small negative values of $\langle uv \rangle_i$ are observed in the region of $0.18 < \xi < 0.25$. This suggests that the negative value of $\overline{uv}$ in the region of $0.18 < \xi < 0.25$ (figure 8) may be produced in the irrotational ambient region outside the turbulent/irrotational interface. The generation mechanism of the negative $\overline{uv}$ will be discussed later with respect to pattern-averaged data measured at two points.

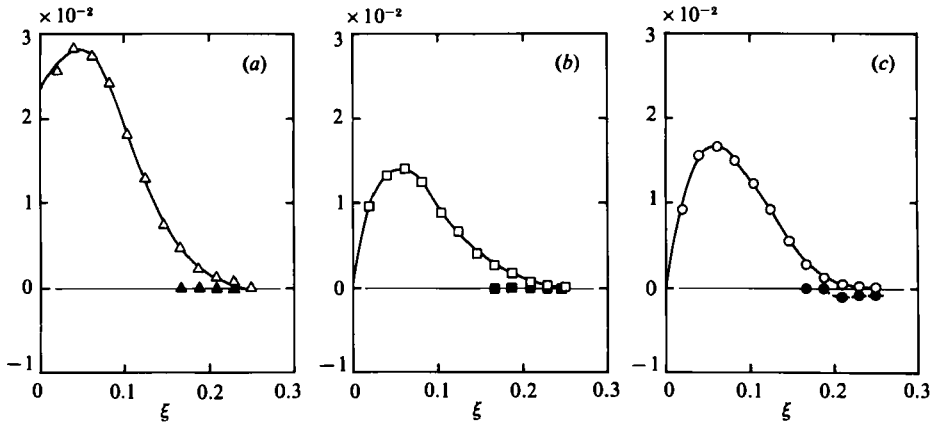

FIGURE 9. Radial distributions of turbulent and irrotational zone-averaged axial and radial heat and momentum fluxes:
(*a*) axial heat flux; △, $\langle u\theta\rangle_t/[(\overline{U}_c-\overline{U}_a)(\overline{T}_c-\overline{T}_a)]$; ▲, $\langle u\theta\rangle_i/[(\overline{U}_c-\overline{U}_a)(\overline{T}_c-\overline{T}_a)]$;
(*b*) radial heat flux; □, $\langle v\theta\rangle_t/[(\overline{U}_c-\overline{U}_a)(\overline{T}_c-\overline{T}_a)]$; ■, $\langle v\theta\rangle_i/[(\overline{U}_c-\overline{U}_a)(\overline{T}_c-\overline{T}_a)]$;
(*c*) Reynolds stress; ○, $\langle uv\rangle_t/(\overline{U}_c-\overline{U}_a)^2$; ●, $\langle uv\rangle_i/(\overline{U}_c-\overline{U}_a)^2$.

4.3. *A coherent structure educed by a pattern-averaged technique*

Shape of the turbulent/irrotational interface at the occurrence of a coherent structure

In order to clarify the existence of a coherent structure and its shape, the spatial correlations between the intermittency function $I(t)$ at a moving measurement position and the intermittency function $I_{p,f}(t)$ or $I(t)$ at a reference measuring position, $\langle I\rangle_p$ and $\langle I\rangle_t$, are calculated and their contours are shown in figures 10(*a*) and (*b*). The correlations $\langle I\rangle_p$ and $\langle I\rangle_t$ are defined by

$$\langle I\rangle_p = \overline{I_m(t)\,I_{p,f}(t)}/\overline{I_{p,f}(t)}, \tag{17}$$

$$\langle I\rangle_t = \overline{I_m(t)\,I_f(t)}/\overline{I_f(t)}. \tag{18}$$

$I_m(t)$ and $I_f(t)$ denote the intermittency function $I(t)$ at a moving measurement point and at a reference measurement point, respectively. In the figures a small circle denotes the location of the reference point, $\bar{x}/d = 47.5$ and $\xi = 0.18$, and it will be used in subsequent figures as well. Also, the contours were determined by interpolating the values measured with a separation distance of 0.01 m in the axial (x-) and radial (r-)directions. To interpolate a value at an arbitrary point in a square mesh formed by 4 measuring points with a distance of 0.01 m, a third-order Lagrange-interpolating polynomial was applied to 16 measuring points which enclose the square. This interpolating method was used for all the contours in subsequent figures.

The contours of $\langle I\rangle_p$ in figure 10(*a*) are strongly skewed towards the irrotational region, compared with those of $\langle I\rangle_t$; and, outside the contour of $\langle I\rangle_p = 0.5$ (shown by a dot-dash line), $\langle I\rangle_p$ decreases rapidly. These skewed contours suggest the existence of a coherent structure which consists of outward turbulent motion towards the irrotational region. The concentrated contours around $\langle I\rangle_p = 0.5$ can be regarded as the spatial shape of a turbulent/irrotational interface at the time when the coherent structure occurs. Also, as will be discussed later, this can be confirmed from the fact that the contour of $\langle uv\rangle_p = 0$ coincides with that of $\langle I\rangle_p = 0.5$.

In contrast, the contours of $\langle I\rangle_t$ are smoother and never suggest the existence of

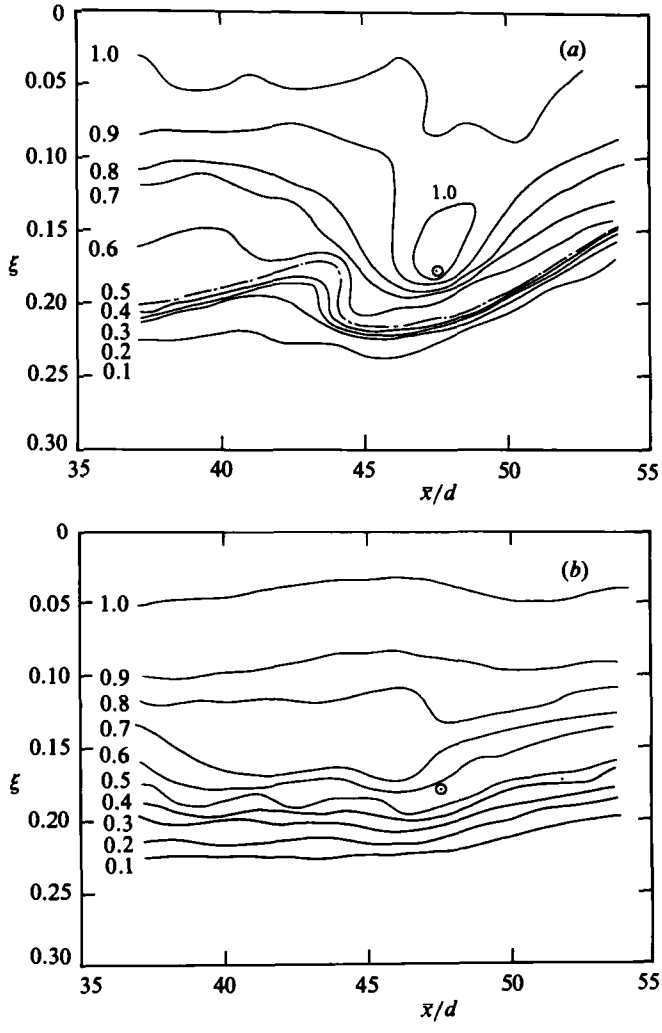

FIGURE 10. Contours of the spatial correlations: (*a*) $\langle I\rangle_p$; (*b*) $\langle I\rangle_t$; ⊙ denotes the reference measurement position, and this symbol will be used in subsequent figures.

the coherent structure. This is attributed to the zone-averaging technique which disperses the shape of the coherent structure.

Pattern-averaged velocities

Figures 11(*a*), (*b*) and (*c*) show the contours of the pattern-averaged velocities, $\langle U\rangle_p - \overline{U}_a$ (axial) and $\langle V\rangle_p$ (radial), and the velocity vectors

$$\overline{U}_p (= (\langle U\rangle_p - \overline{U}_a, \langle V\rangle_p)),$$

respectively. In each figure, a dot-dash line denotes the turbulent/irrotational interface of $\langle I\rangle_p = 0.5$ shown in figure 10(*a*). The directions of the velocity vector $\overline{U}_p$ are denoted by the orientations of the arrows, the magnitudes by the line lengths and the sizes of the head of the arrow, and the origins by the initial edges of the arrow. In the outer region of $0.1 < \xi < 0.2$ the contours of the large positive $\langle U\rangle_p$ and $\langle V\rangle_p$

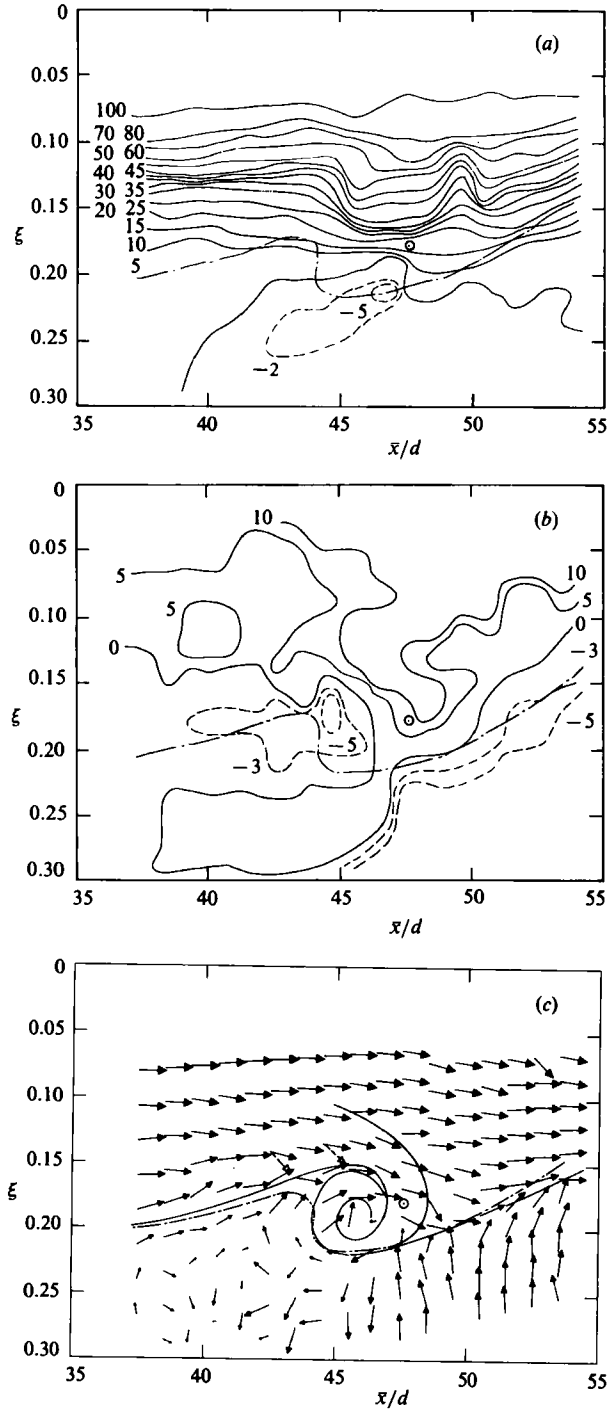

FIGURE 11. Contours of pattern-averaged velocities and the velocity vectors:
(*a*) pattern-averaged axial velocity $(\langle U\rangle_p-\overline{U}_a)/(\overline{U}_c-\overline{U}_a)\times 200$;
(*b*) pattern-averaged radial velocity $\langle V\rangle_p/(\overline{U}_c-\overline{U}_a)\times 200$;
(*c*) velocity vectors $\overline{U}_p[=(\langle U\rangle_p-\overline{U}_a, \langle V\rangle_p)]$;
— — —, jet-boundary of $\langle I\rangle_p=0.5$; ——, line representing a vortical structure; ⊙ as in figure 10.

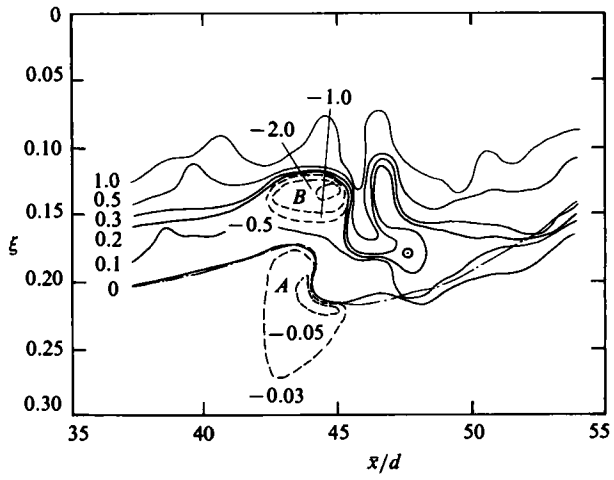

FIGURE 12. Contours of the pattern-averaged Reynolds stress $\langle uv\rangle_p/(\overline{U}_c-\overline{U}_a)^2\times 100$: ———, jet-boundary of $\langle I\rangle_p = 0.5$; – – – –, the negative Reynolds stress contours; ⊙ as in figure 10.

stretch towards the reference measurement position near the interface, suggesting the presence of strong outward turbulent motion from inside the jet towards the reference position. Both outside and inside the turbulent bulge shown by the convex interface, the relative velocity $\langle U\rangle_p - \overline{U}_a$ becomes negative. Around the base (concave) region of the bulge, negative $\langle V\rangle_p$ is observed. These observations mean that vortical flow-reversal towards the ambient stream and inflow into the jet simultaneously appear in the region near the bulgy interface when the strong outward motion occurs from inside the jet, and that the vortical inflow in the irrotational zone is instantaneously induced via pressure forces by the large-scale vortical motion in the turbulent zone. This coherent vortical structure can be seen more clearly in the distributions of the velocity vectors (figure 11*c*). In particular, roll-up by both the reverse flow in the turbulent zone and the inflow in the irrotational zone is remarkable in the region $43 < \bar{x}/d < 47$, and the outward turbulent flow towards the reference position can be observed clearly. The outward turbulent flow impinging on the interface (irrotational fluid) is split into two parts near the upstream region of the reference position. One part turns around to form a reverse motion. The other part seems to constitute a roll-up motion in the downstream vortical structure which may become organized in the region, $\bar{x}/d > 55$. From the spatial interval between these vortical structures, the size of a coherent structure is estimated to be $15d$.

Pattern-averaged Reynolds stress

Figure 12 shows the contours of the pattern-averaged Reynolds stress $\langle uv\rangle_p$ which are averaged only when the coherent structure (figure 11) occurs. The contour of $\langle uv\rangle_p = 0$ is in good agreement with the turbulent/irrotational interface of $\langle I\rangle_p = 0.5$. In the irrotational ambient region outside the interface, $\langle uv\rangle_p$ is almost equal to zero, except for the area denoted by A in the figure. In the irrotational A area in front of the bulgy (convex) interface region, the small negative $\langle uv\rangle_p$ is observed. The existence of the negative $\langle uv\rangle_p$ outside the interface well explains the result in figure 9 (*c*) that negative Reynolds stress is generated in the irrotational zone: $\langle uv\rangle_i < 0$. Also, it supports the location of the turbulent/irrotational interface by a dot-dash line in figure 10 (*a*). Inside the interface, almost all turbulent regions show

positive $\langle uv\rangle_p$ in which the large positive contours stretch toward the reference measurement position. In the upstream vicinity of this high-shear region, negative $\langle uv\rangle_p$ is also observed (the B area in the figure). Considering that the coherent structure with the two areas (A and B) of the negative $\langle uv\rangle_p$ intermittently appears and it is carried downstream, we can understand easily the effects of the negative $\langle uv\rangle_p$ on the conventionally averaged or zone-averaged Reynolds stress. As shown in figure 12, the two areas of A and B with the negative $\langle uv\rangle_p$ are rather narrow, compared with the total area of the coherent structure. This means that the time period required for the passage of the A or B area through the measuring points is rather small, compared with the time period for the passage of total coherent structure. Despite such a small time fraction, the effect of the negative $\langle uv\rangle_p$ in the A area located in the irrotational region becomes significant for $\overline{uv}$ and $\langle uv\rangle_t$ in the range of $0.18 < \xi < 0.25$ as shown in figures 8 and 9(c). This is attributed to the fact that the wide irrotational area, except for the A area, has a zero value of $\langle uv\rangle_p$ in the region of $0.18 < \xi < 0.25$ and never affects $\overline{uv}$ and $\langle uv\rangle_t$. On the contrary, the effect of the negative $\langle uv\rangle_p$ in the B area located in the turbulent jet is cancelled by the large positive $\langle uv\rangle_p$ which prevails in the wide turbulent range around the B area (see figure 12). Thus, the sign of $\overline{uv}$ and $\langle uv\rangle_t$ in the region of $0.13 < \xi < 0.16$ never changes (figures 8 and 9c).

In order to clarify the generation mechanism of the above negative $\langle uv\rangle_p$, the signal of the instantaneous Reynolds stress $u_p v_p[\equiv (U-\langle U\rangle_p)(V-\langle V\rangle_p)]$ measured at a moving position was conditionally classified into the four quadrants of the (u_p, v_p)-plane. The classified value was then pattern-averaged by using $I_{p,f}(t)$ in the form of a correlation coefficient. The pattern-averaged correlation value $\langle uv\rangle_{p,i}/(u'_p v'_p)$ in the i quadrant was represented as a vector defined by

$$\boldsymbol{R}_i = |\langle uv\rangle_{p,i}/(u'_p v'_p)|\,[(\delta_{i1}-\delta_{i2}-\delta_{i3}+\delta_{i4})\,\boldsymbol{i}+(\delta_{i1}+\delta_{i2}-\delta_{i3}-\delta_{i4})\,\boldsymbol{j}], \tag{19}$$

where $\boldsymbol{i}$ is the unit vector in the x direction, $\boldsymbol{j}$ the unit vector in the r direction, δ_{ij} the Kronecker delta, and u'_p and v'_p denote the pattern-averaged r.m.s. values of u_p and v_p. The sum of the vectors $\boldsymbol{R}(=\boldsymbol{R}_1+\boldsymbol{R}_2+\boldsymbol{R}_3+\boldsymbol{R}_4)$ is shown by the arrows in figure 13. The direction of the vector is denoted by the orientation of the arrows and the magnitude of the correlation coefficient by the line length. The vectors approximately indicate the direction in which the motion most contributive to the Reynolds stress $\langle uv\rangle_p$ deviates from the pattern-averaged velocity $\overline{\boldsymbol{U}}_p$. The vectors $\boldsymbol{R}$ both in the turbulent high-shear region towards the reference position and in the irrotational-inflow region are in similar directions to the pattern-averaged velocity vectors $\overline{\boldsymbol{U}}_p$ in figure 11 (c). This means that the large positive $\langle uv\rangle_p$ in the high-shear region (figure 12) inside the interface and the small negative $\langle uv\rangle_p$ in the irrotational A region are instantaneously produced when the large-scale vortical motion is strongly accelerated, compared with $\overline{\boldsymbol{U}}_p$. In order to investigate the detailed generation mechanism of the small negative Reynolds stress in the irrotational A region, each term in the transport equation of the Reynolds stress must be estimated by experiments. Even if the dissipation and diffusion terms are neglected there, this task is difficult because of lack of pressure fluctuation measurements. However, when considering that velocity fluctuation and small negative velocity gradient $(\partial\langle U\rangle_t/\partial r)$ in the present irrotational flow between the turbulent bulges are produced via pressure forces by the large-scale turbulent bulgy motion inside the interface, we can expect that the pressure–strain correlation term acts to produce the small negative Reynolds stress. In general, the shear production term gives a positive contribution to the Reynolds stress and the pressure-strain term a negative contribution. In the

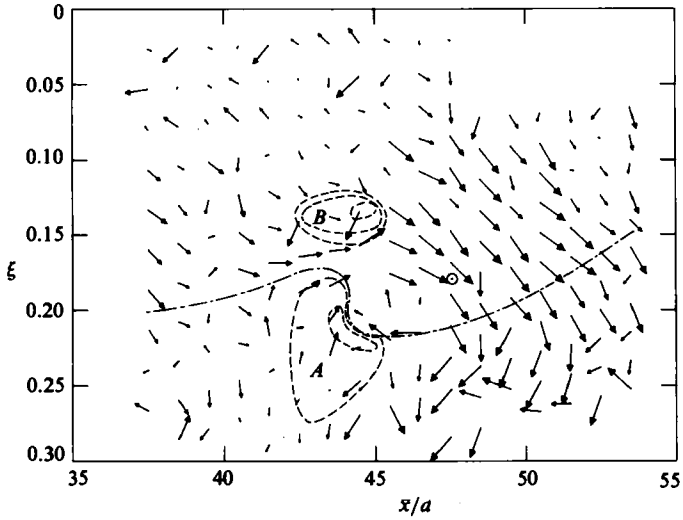

FIGURE 13. Vectors of the correlation coefficients of classified, pattern-averaged Reynolds stress; — — —, jet boundary of $\langle I\rangle_p = 0.5$; – – –, the negative Reynolds stress region in figure 12; ⊙ as in figure 10.

present irrotational flow with the small velocity gradient, the pressure-strain term may exceed the shear production term. Contrary to the present result, Phillips (1955) studied the motion in the irrotational region, set up a randomly disturbed velocity field at an interface, and theoretically found that the Reynolds stress was never produced in the irrotational region. In his theory, the following relation must be satisfied in neighbourhood of the interface

$$\langle u_2^2\rangle_i = \langle u_1^2\rangle_i + \langle u_3^2\rangle_i, \tag{20}$$

where u_2 is the velocity fluctuation normal to the interface. Experimentally, Townsend (1949) and Wygnanski & Fiedler (1970) verified the above relation in a turbulent wake of a circular cylinder and in a two-dimensional mixing layer. However, their velocity measurements by hot-wire anemometry in the irrotational region are uncertain, as mentioned in §4.1. Contrary to their measurements, the present experimental results never satisfy the above relation. In the present experiments, $\langle v^2\rangle_i$ is approximately equal to $1.2\langle u^2\rangle_i$ at the averaged location ($\xi = 0.18$) of the interface. If the relation (20) is satisfied, $\langle w^2\rangle_i$ must be equal to $0.2\langle u^2\rangle_i$. Although tangential velocity fluctuation w was not measured in the present experiments, it is easily understood that such a small value of $\langle w^2\rangle_i$ is quite unreasonable. Of course, for a round jet, u_2 is not exactly equal to the radial velocity v, but v can be approximately regarded as u_2 in the region far from the jet nozzle and jet axis ($\bar{x}/d = 47.5$, $\xi = 0.21$). This discrepancy between the present measurements and the Phillips's result may be attributed to a significant assumption of the homogeneity of the irrotational flow in the x_1- (x-)direction. This assumption may be suitable for the irrotational flow in two-dimensional boundary layer. However, in a self-preserving round jet, mean statistical properties vary as x^{-1}, and the irrotational inflow between the turbulent bulges is strongly affected via pressure forces by the large-scale turbulent motion inside the interface. In such irrotational inflow, homogeneity in the x-direction will never be attained. Thus, the disagreement between the Phillips's result and the present measurements seems to support the

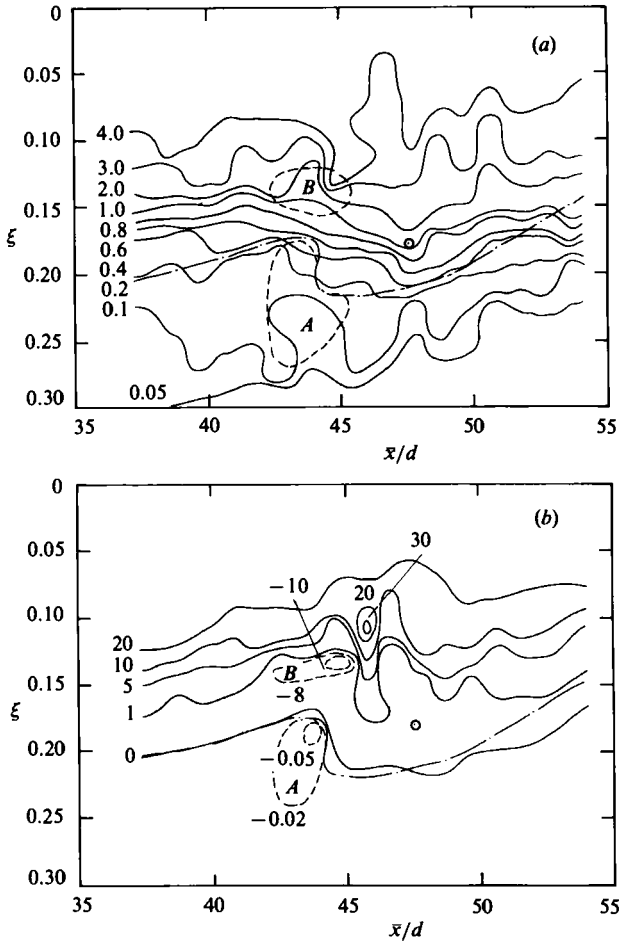

FIGURE 14. Contours of pattern-averaged turbulence kinetic energy and the turbulence production term: (*a*) pattern-averaged kinetic energy $\langle q^2\rangle_p/(\overline{U}_c-\overline{U}_a)^2\times 40$; (*b*) pattern-averaged production term $\langle uv\rangle_p(\partial\langle U\rangle_p/\partial r)\,d/(\overline{U}_c-\overline{U}_a)^3\times 10000$; ———, jet boundary of $\langle I\rangle_p=0.5$; – – – –, the negative Reynolds stress region in figure 12 or the negative production region; ⊙ as in figure 10.

possibility that the Reynolds stress is produced in the irrotational region of a round jet.

In the *B* area with the negative $\langle uv\rangle_p$, the directions of the two vectors $\boldsymbol{R}$ are quite different from those of $\overline{\boldsymbol{U}}_p$ in figure 11 (*c*). Here, it should be noted that the direction of $\boldsymbol{R}$ does not mean the instantaneous motion opposite to $\overline{\boldsymbol{U}}_p$, but approximately indicates the direction which the motion most contributive to $\langle uv\rangle_p$ deviates from $\overline{\boldsymbol{U}}_p$. To determine the certain velocity vector $\boldsymbol{U}$ of the instantaneous motion most contributive to $\langle uv\rangle_p$, the magnitude of the vector $\boldsymbol{U}-\overline{\boldsymbol{U}}_p(=m\boldsymbol{R}/|R|)$ must be estimated, where $|R|$ is a magnitude of $\boldsymbol{R}$. Substituting $(u_p'^2+v_p'^2)^{\frac{1}{2}}$ for m, two vectors $\boldsymbol{U}$ in the *B* region shown by dashed arrows in figure 11 (*c*) are approximately obtained. The two dashed arrows show that the negative Reynolds stress is instantaneously produced when the turbulent motion in the *B* area is more strongly directed towards the centre of the vortical structure than the averaged motion. This suggests that the turbulent fluid in the *B* region is drawn strongly into the clockwise vortical motion along the solid line (under the *B* region) sketched in figure 11 (*c*), when the vortical motion is accelerated.

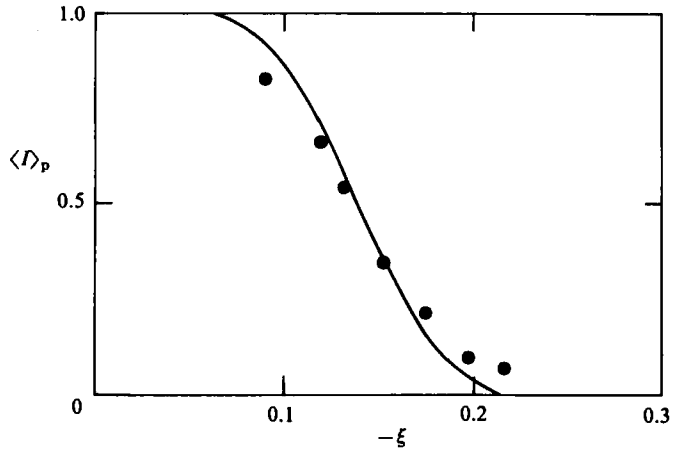

FIGURE 15. Distributions of pattern-averaged intermittency factor $\langle I\rangle_p$ against negative ξ: ●, $\langle I\rangle_p$ against $-\xi$; ——, best-fit curve of the intermittency factor f against ξ in figure 4.

Hussain & Zaman (1980) have also observed the similar coherent negative values of the phase-averaged Reynolds stress in the near field of a round jet. However, comparison with our results in the self-preserving region is difficult, since the interface and the similarity were not clearly defined.

Pattern-averaged turbulence kinetic energy

Contours of the pattern-averaged turbulence kinetic energy

$$\langle q^2\rangle_p (\equiv \langle u^2\rangle_p + 2\langle v^2\rangle_p)$$

and the turbulence production term $\langle uv\rangle_p (\partial\langle U\rangle_p/\partial r)$ are plotted in figures 14(*a*) and (*b*), respectively. The contours of $\langle q^2\rangle_p$ stretch towards the reference position from inside the jet, and, near the reference position, the turbulence level becomes relatively high. This is due to high turbulence production downstream of the *B* area (figure 14*b*). In the *A* and *B* areas of negative $\langle uv\rangle_p$ (enclosed by the dashed lines), the level of $\langle q^2\rangle_p$ is small, since the negative production term, $\langle uv\rangle_p (\partial\langle U\rangle_p/\partial r)$, promotes a reduction in turbulence energy (see figure 14*b*). However, to the right of the *B* area, the level of $\langle q^2\rangle_p$ is high despite the existence of negative production. From a turbulent-energy budget, this elevated region was found to be owing to the diffusion of kinetic energy into the *B* region from the high Reynolds stress region downstream.

Symmetry of the coherent structure

In order to investigate the symmetry of the coherent structure with respect to the axis, the pattern-averaged intermittency factor $\langle I\rangle_p$ defined by (17) was calculated on the $(x, -r)$-plane, where negative r denotes radial distance from the axis in the symmetric direction with respect to the reference point. The values of $\langle I\rangle_p$ are plotted against the negative $\xi(=-r/\bar{x})$ in figure 15. In the outer intermittent region of $-\xi \gtrsim 0.18$, the values of $\langle I\rangle_p$ are almost the same or slightly larger than the best-fit curve of the intermittency factor f plotted against positive ξ in figure 4. This means that motion in the region of negative ξ is quite independent of the coherent motion at the reference position. That is, the symmetry of the present coherent structure is very weak and the present structure is not similar to the coherent structure of a vortex ring observed in the near field.

5. Conclusions

The coherent structure in the almost self-preserving region of a round free jet has been experimentally investigated by using both pattern-averaging and two-point measuring techniques. The main results from this study can be summarized as follows.

(1) A large-scale coherent vortical structure exists in the self-preserving region as well as in the near field. The vortical structure consists of strong outward turbulent motion from inside the jet, turbulent reverse motion and inflow in the ambient irrotational region (entrainment).

(2) Two areas with negative pattern-averaged Reynolds stress are present in the coherent structure: one occurs in the irrotational ambient region outside the bulgy turbulent/irrotational interface; the other is in the turbulent zone near the high-shear region. The former is instantaneously produced in the irrotational inflow when the vortical motion which includes the inflow is accelerated, and it results in negative values of the conventionally averaged Reynolds stress in the outer region. The latter is produced instantaneously in the turbulent flow near the high-shear region when the turbulent outward motion is more strongly directed by the acceleration of the vortical motion towards the centre of the vortical structure than the averaged motion. This negative pattern-averaged Reynolds stress does not change the sign of the conventionally averaged stress, since the effect of the negative stress is cancelled by the large positive Reynolds stress which prevails in the wide turbulent range around the negative-stress area.

We would like to thank Professor K. Yamamoto for his continuing interest in this work and Mr Y. Koizumi for his assistance in conducting the experiments.

REFERENCES

Antonia, R. A., Prabhu, A. & Stephenson, S. E. 1975 Conditionally sampled measurements in a heated turbulent jet. *J. Fluid Mech.* **72**, 455–480.

Bendat, J. S. & Piersol, A. G. 1971 *Random Data: Analysis and Measurement Procedures.* New York: Wiley-Interscience.

Bruun, H. H. 1977 A time-domain analysis of the large-scale flow structure in a circular jet. *J. Fluid Mech.* **83**, 641–671.

Chevray, R. & Tutu, N. K. 1978 Intermittency and preferential transport of heat in a round jet. *J. Fluid Mech.* **88**, 133–160.

Corrsin, S. 1943 Investigation of flow in an axially symmetric heated jet of air. *NACA Rep. no.* W-94.

Durst, F., Melling, A. & Whitelaw, J. H. 1976 *Principles and Practice of Laser-Doppler Anemometry.* Academic.

Hussain, A. K. M. F. & Zaman, K. B. M. Q. 1980 Vortex pairing in a circular jet under controlled excitation. Part 2. Coherent structure dynamics. *J. Fluid Mech.* **101**, 493–544.

Hussain, A. K. M. F. & Zaman, K. B. M. Q. 1981 The preferred mode of the axisymmetric jet. *J. Fluid Mech.* **110**, 39–71.

Komori, S. & Ueda, H. 1984 Turbulent effects on the chemical reaction for a jet in a non-turbulent stream and for a plume in a grid-generated turbulence. *Phys. Fluids* **27**, 77–86.

Komori, S., Ueda, H., Ogino, F. & Mizushina, T. 1982 Turbulence structure in unstably-stratified open-channel flow. *Phys. Fluids* **25**, 1539–1546.

Komori, S., Ueda, H., Ogino, F. & Mizushina, T. 1983 Turbulence structure in stably stratified open-channel flow. *J. Fluid Mech.* **130**, 13–26.

Melling, A. & Whitelaw, J. H. 1975 Optical and flow aspects of particles. In *Proc. of LDA-75 Symp., Copenhagen*, pp. 382–402.

MIZUSHINA, T., OGINO, F., UEDA, H. & KOMORI, S. 1979 Application of laser Doppler velocimetry to turbulence measurement in non-isothermal flow. *Proc. R. Soc. Lond.* A **366**, 63–79.

PHILLIPS, O. M. 1955 The irrotational motion outside a free turbulent boundary. *Proc. Camb. Phil. Soc.* **51**, 220–229.

SREENIVASAN, K. R., ANTONIA, R. A. & BRITZ, D. 1979 Local isotropy and large structures in a heated turbulent jet. *J. Fluid Mech.* **94**, 745–775.

TOWNSEND, A. A. 1949 The fully developed turbulent wake of a circular cylinder. *Austral. J. Sci. Res.* **2**, 451–468.

WYGNANSKI, I. & FIEDLER, H. 1969 Some measurements in the self-preserving jet. *J. Fluid Mech.* **38**, 577–612.

WYGNANSKI, I. & FIEDLER, H. 1970 The two-dimensional mixing region. *J. Fluid Mech.* **41**, 327–361.

WYGNANSKI, I. & OSTER, D. 1980 A forced, plane, turbulent mixing-layer: a challenge for the predictor. In *Turbulent shear flows 2*, p. 314. Springer.

YULE, A. J. 1978 Large-scale structure in the mixing layer of a round jet. *J. Fluid Mech.* **89**, 413–432.